Defence Research and Development Canada
Recherche et développement pour la défense Canada

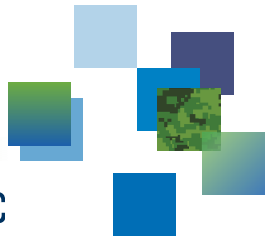

DRDC | RDDC
technologysciencetechnologie

Turbulence variability in hyper-spectral imagery

G. Potvin
DRDC – Valcartier Research Centre

Defence Research and Development Canada
Scientific Report
DRDC-RDDC-2018-R257
November 2018

Canada

IMPORTANT INFORMATIVE STATEMENTS

This document was reviewed for Controlled Goods by DRDC using the Schedule to the *Defence Production Act*.

Disclaimer: Her Majesty the Queen in right of Canada, as represented by the Minister of National Defence ("Canada"), makes no representations or warranties, express or implied, of any kind whatsoever, and assumes no liability for the accuracy, reliability, completeness, currency or usefulness of any information, product, process or material included in this document. Nothing in this document should be interpreted as an endorsement for the specific use of any tool, technique or process examined in it. Any reliance on, or use of, any information, product, process or material included in this document is at the sole risk of the person so using it or relying on it. Canada does not assume any liability in respect of any damages or losses arising out of or in connection with the use of, or reliance on, any information, product, process or material included in this document.

Endorsement statement: This publication has been peer-reviewed and published by the Editorial Office of Defence Research and Development Canada, an agency of the Department of National Defence of Canada. Inquiries can be sent to: Publications.DRDC-RDDC@drdc-rddc.gc.ca.

© Her Majesty the Queen in Right of Canada, Department of National Defence, 2018

© Sa Majesté la Reine en droit du Canada, Ministère de la Défense nationale, 2018

Abstract

Hyper-Spectral Imaging (HSI) is subject to adverse atmospheric effects such as aerosols, gas mixtures and turbulence. Although aerosol and gas mixture effects on HSI performance have been studied, little is known about optical turbulence effects on HSI spectral variability.

This has now been investigated by propagating coherent beams at various central wavelengths and spectral bandwidths in the aero-ballistic range at the DRDC – Valcartier Research Centre, and propagating them through artificially generated optical turbulence. Image sequences of the beam were recorded with a panchromatic camera, and the turbulent variance of the total irradiance of the beams as a function of central wavelength and bandwidth were estimated.

A simple model for the spectral covariance induced by turbulence was developed that compares reasonably well with the measured variances at various central wavelengths and bandwidths. This result gives some confidence in our model, which predicts potentially significant loss of correlation for Visible and Near Infra-Red (VNIR) and Short Wave Infra-Red (SWIR) spectra. It is concluded that turbulence effects could have a significant impact on HSI target identification and that further study is required.

Significance for defence and security

Hyper-Spectral Imaging (HSI) is a very important remote sensing method for a variety of applications. Like all imaging systems, HSI systems can be adversely affected by the intervening atmosphere to a target of interest. While atmospheric effects such as absorption by aerosols and gas mixtures are well known, very little is known about the effects of turbulence on HSI performance. This report examines the spectral variability created by turbulence with a view towards assessing its possible effect on target detection algorithms for HSI systems.

Résumé

L'imagerie hyper-spectrale (HSI : Hyper-Spectral Imaging) est sujette à des effets atmosphériques défavorables tels que les aérosols, les mélanges de gaz et les turbulences. Bien que les effets des mélanges d'aérosols et de gaz sur les performances de systèmes HSI aient été étudiés, les effets de la turbulence optique sur la variabilité spectrale pour le HSI sont peu connus.

Ces effets ont été étudié en propageant des faisceaux cohérents à diverses longueurs d'onde centrales et bandes passantes spectrales dans le couloir aéro-balistique du RDDC - Centre de recherches de Valcartier, et en les propageant à travers la turbulence optique générée artificiellement. Les séquences d'images du faisceau ont été enregistrées avec une caméra panchromatique, et la variance turbulente de l'irradiance totale des faisceaux en fonction de la longueur d'onde centrale et de la bande passante a été estimée.

Un modèle simple pour la covariance spectrale induite par la turbulence fut développé qui se compare raisonnablement bien avec les variances mesurées à diverses longueurs d'onde centrales et largeurs de bande. Ce résultat donne une certaine confiance dans notre modèle, qui prédit une perte potentiellement importante de corrélation pour les spectres VNIR (Visible and Near Infra-Red) et SWIR (Short Wave Infra-Red). Nous concluons que les effets de la turbulence pourraient avoir un impact significatif sur l'identification des cibles pour le HSI et qu'une étude plus approfondie est nécessaire.

Importance pour la défense et la sécurité

L'imagerie hyper-spectrale (HSI : Hyper-Spectral Imaging) est une méthode de télédétection très importante pour une variété d'applications. Comme tous les systèmes d'imagerie, les systèmes HSI peuvent être affectés négativement par l'atmosphère intermédiaire à une cible d'intérêt. Alors que les effets atmosphériques tels que l'absorption par les aérosols et les mélanges de gaz sont bien connus, on en sait très peu sur les effets de la turbulence sur les performances de systèmes HSI. Ce rapport examine la variabilité spectrale induite par la turbulence en vue d'évaluer son effet possible sur les algorithmes de détection de cibles pour les systèmes HSI.

Acknowledgements

The author would like to gratefully acknowledge the assistance of Martin Bérubé from the DRDC – Valcartier Research Centre in setting up the apparatus and in collecting the turbulent beam data.

This page intentionally left blank.

Table of contents

List of figures

1 Introduction

The average effects of turbulence on hyper-spectral imaging has previously been investigated by propagating a coherent beam through artificial turbulence created by a series of heating elements [1]. A coherent target was used to accentuate the average effect of turbulence, as demonstrated by its theoretical analysis. It was found that turbulence can alter the average transmittance over the combined Visible and Near Infra-Red (VNIR) spectrum by about 5% according to the theory, compared to a measured difference of 9%. Since these conditions were considered extreme, both in terms of turbulence strength and target coherence, it was concluded that turbulence will only have a minimal average effect under most imaging conditions.

This report examines the spectral variance created by turbulence and its effect on Hyper-Spectral Imaging (HSI) system target detection algorithms that depend on properly characterizing the variance and covariance values of the measured spectra [2, 3, 4]. This variability in the spectra created by turbulence could therefore potentially significantly reduce the performance of these algorithms.

To investigate this possible effect on algorithm performance, a trial looking at the effect of turbulent variability was carried out at the Aero-Ballistic range (AB-range) at DRDC – Valcartier Research Centre. To interpret the measurements presented in Chapter 3, a simple model regarding turbulent variability was developed and is presented in Chapter 2. Results and conclusions from this work and for future work are given in Chapter 4.

2 The model

2.1 Fundamentals

A complete model for the turbulence induced variance on hyper-spectral imagery would require that the fourth-order *Mutual Coherence Function* (MCF) of the propagating electric field be modeled. However, obtaining a detailed expression for the fourth-order MCF is quite difficult (see for instance Strohbehn [5]). Therefore, a model that reduces the problem to its simplest expression, namely a point source emitting a broad spectrum of radiation through optically weak turbulence to a point receiver, as illustrated in Fig. 1, is developed.

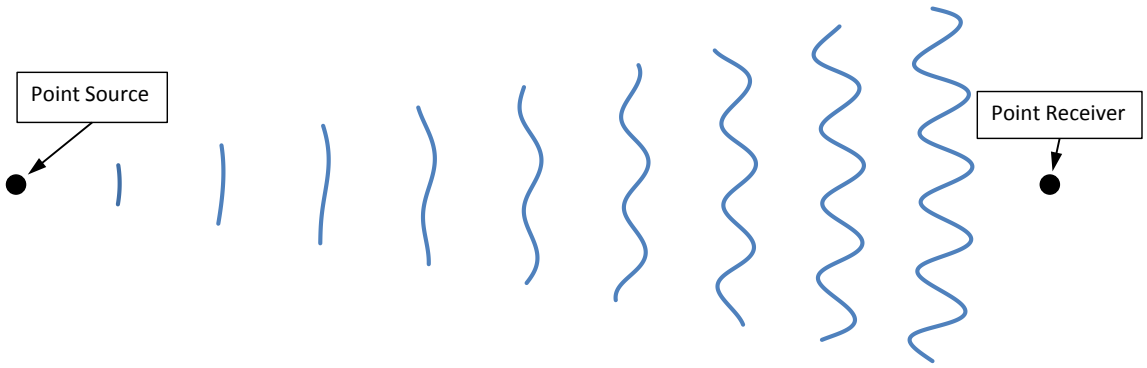

Figure 1: *Illustration of the spectral variance model. The point source on the left emits wavefronts towards the point receiver on the right. As they propagate through turbulence the wavefronts become progressively more distorted.*

Assuming that the receiver is a distance L from the source, and that this distance is along the z-axis of our system of coordinates, the electric field arriving at the receiver plane $(\vec{\rho}, L)$, where $\vec{\rho} = (x, y)$, and the source is located at the origin, is given as:

$$E\left(\vec{\rho}, L\right) = E_0\left(\vec{\rho}, L\right) \exp\left[\chi + iS\right] , \tag{1}$$

where:

$$E_0\left(\vec{\rho}, L\right) = \frac{k}{2\pi i L} \exp\left[ikL + \frac{ik}{2L}\rho^2\right] , \tag{2}$$

is the paraxial approximation of a spherical wave with wavenumber $k = 2\pi/\lambda$. The fields $\chi(\vec{\rho}, L)$ and $S(\vec{\rho}, L)$ are the respective turbulent log-amplitude and phase perturbations of the wave. The refractive index of the turbulent air is $n = 1 + n_1$, where $n_1 \ll 1$ is a small perturbation of the refractive index and is the cause of χ and S. The Rytov representation can be expanded as a sum [6, 7, 8, 9, 10, 11]:

$$\chi = \sum_{m=1}^{\infty} \chi_m , \quad S = \sum_{m=1}^{\infty} S_m , \tag{3}$$

where χ_1 is the first-order perturbation in n_1, χ_2 is the second-order perturbation in n_1 and so on. The first-order Rytov approximation is $\chi \approx \chi_1$ and $S \approx S_1$, which is valid for weak turbulence. The first-order log-amplitude and phase perturbations are given by:

$$\chi_1(\vec{\rho}, L, k) = kL \int_0^1 \mathrm{d}\eta \int \mathrm{d}^2K\, N_1\left(\vec{K}, L\eta\right) \exp\left[i\vec{K}\cdot\vec{\varrho}\eta\right] \sin\left[\frac{K^2L}{2k}\eta(1-\eta)\right], \tag{4}$$

and:

$$S_1(\vec{\rho}, L, k) = kL \int_0^1 \mathrm{d}\eta \int \mathrm{d}^2K\, N_1\left(\vec{K}, L\eta\right) \exp\left[i\vec{K}\cdot\vec{\varrho}\eta\right] \cos\left[\frac{K^2L}{2k}\eta(1-\eta)\right]; \tag{5}$$

where $\eta = z/L$ is a normalized coordinate along the line-of-sight axis z and where:

$$N_1\left(\vec{K}, z\right) = \left(\frac{1}{2\pi}\right)^2 \int \mathrm{d}^2\rho\, n_1(\vec{\rho}, z) \exp\left[-i\vec{K}\cdot\vec{\rho}\right] \tag{6}$$

is the Fourier transform of the refractive index perturbation over the x-y plane with the vector $\vec{K}$ as the wavenumber. The sine function in Eq. (4) indicates that mainly eddies the size of a Fresnel zone ($\mu = \sqrt{\lambda L}$) will contribute to the log-amplitude fluctuations, whereas the cosine in Eq. (5) tells us that large eddies, the size of the outer scale, contribute to the phase fluctuations.

The irradiance arriving at the receiver is proportional to the absolute value squared of the electric field, $I \propto |E|^2$. For a point source and a point receiver, neither the phase fluctuations or aperture averaging at either end of the line-of-sight need to be considered, such that, using Eq. (1):

$$I(k) \propto \exp\left[2\chi(k)\right]. \tag{7}$$

Assuming that the turbulent refractive index fluctuation is normally distributed, it follows from Eq. (4) that χ is also normally distributed. In this case, the average irradiance at the receiver is given by:

$$\langle I(k)\rangle \propto \exp\left[2\langle\chi(k)\rangle + 2\sigma_\chi^2(k)\right] \tag{8}$$

where the angle brackets represent the average over the turbulent fluctuations and $\sigma_\chi^2(k)$ is the variance of $\chi(k)$. Also assuming that the turbulent refractive index fluctuations average to zero, $\langle n_1\rangle = 0$, then the log-amplitude fluctuation also averages to zero, $\langle\chi(k)\rangle = 0$. But from Eq. (8), it would seem that the turbulent fluctuations increase the amount of irradiance entering the receiver. This would make it appear as though the turbulence in the atmosphere increases the amount of energy emitted by the source, which is unphysical since a transparent atmosphere is supposed. This is the result of neglecting the higher-order terms of the expansion. The energy increase is corrected by setting [10] $\langle\chi(k)\rangle = -\sigma_\chi^2(k)$, so that $\chi \approx \chi_1 - \sigma_{\chi_1}^2$ and $\langle I(k)\rangle \propto 1$ as needed.

2.2 Covariance and correlation

Now assuming that the source is emitting over a broad band of wavelengths and that the receiver is sensitive over that same band, the covariance between the irradiance received at the wavelengths λ and λ' (where $k' = 2\pi/\lambda'$) is:

$$C_I(\lambda, \lambda') = \langle I(\lambda) I(\lambda') \rangle - \langle I(\lambda) \rangle \langle I(\lambda') \rangle \,, \tag{9}$$

which becomes:

$$\begin{aligned} C_I(\lambda, \lambda') &\propto \langle \exp\left[2\chi(\lambda) + 2\chi(\lambda')\right] \rangle - 1 \,, \\ &\propto \exp\left[4C_\chi(\lambda, \lambda')\right] - 1 \,, \end{aligned} \tag{10}$$

where:

$$C_\chi(\lambda, \lambda') = \langle (\chi(\lambda) - \langle \chi(\lambda) \rangle)(\chi(\lambda') - \langle \chi(\lambda') \rangle) \rangle \,, \tag{11}$$

is the covariance for the log-amplitude fluctuations. If the log-amplitude variance is sufficiently small, then $C_I \approx 4C_\chi$.

Upon substituting Eq. (4) into Eq. (11), the log-amplitude covariance becomes:

$$\begin{aligned} C_\chi(\lambda, \lambda') = k k' L^2 \int_0^1 \mathrm{d}\eta \int_0^1 \mathrm{d}\eta' \int \mathrm{d}^2 K \int \mathrm{d}^2 K' \\ \times \left\langle N_1\left(\vec{K}, L\eta\right) N_1^*\left(\vec{K}', L\eta'\right) \right\rangle \sin\left[\frac{K^2 L}{2k}\eta(1-\eta)\right] \sin\left[\frac{K'^2 L}{2k'}\eta'(1-\eta')\right] . \end{aligned} \tag{12}$$

Optical turbulence can be thought of as having an outer scale, L_0, that can be regarded as the largest scale size for which local homogeneity and isotropy are reasonable, the scale size of the energy source, or as the dimension of the flow as a whole [10]. If the outer scale is much smaller than the path length, $L_0 \ll L$, then the covariance of the refractive index Fourier transform [12] becomes:

$$\left\langle N_1\left(\vec{K}, L\eta\right) N_1^*\left(\vec{K}', L\eta'\right) \right\rangle \approx \frac{2\pi}{L} \Phi_n\left(\frac{\vec{K} + \vec{K}'}{2}, 0\right) \delta\left(\vec{K} - \vec{K}'\right) \delta\left(\eta - \eta'\right) \,, \tag{13}$$

where $\Phi_n(\vec{K}, K_z)$ is the three-dimensional power spectrum for the turbulent refractive index fluctuations. This is usually taken to be a modified form of the Kolmogorov turbulent power spectrum [12] :

$$\Phi_n(\vec{K}, K_z) = 0.033\, C_n^2 \frac{\Gamma\left(l_0 \sqrt{K^2 + K_z^2}\right)}{\left(K_0^2 + K^2 + K_z^2\right)^{11/6}} \,, \tag{14}$$

where $K_0 = 2\pi/L_0$ is the turbulent wavenumber corresponding to the outer scale and C_n^2 is the refractive index structure function parameter. The function Γ suppresses the spectrum for scales smaller than the inner scale l_0, which represents the scale at which dissipation predominates and therefore is roughly the size of the smallest turbulent eddies. A form proposed by Churnside [13] is used, which is designed to model a 'bump' in the

spectrum around the inner scale that has been observed by Williams and Paulson [14] and by Champagne *et* al. [15]:

$$\Gamma\left(x\right)=\exp\left[-1.28x^{2}\right]+1.45\exp\left[-0.97\left(\ln\left(x\right)-0.45\right)^{2}\right]. \tag{15}$$

This function has a bump around $x\approx 1$, it tends to zero for a large argument ($\Gamma\to 0$ for $x\gg 1$), and tends to unity for a small argument ($\Gamma\to 1$ for $x\ll 1$). Now, placing Eq. (13) in Eq. (12), gives:

$$C_{\chi}\left(\lambda,\lambda'\right)=2\pi kk'L\int_{0}^{1}\mathrm{d}\eta\int\mathrm{d}^{2}K \times\Phi_{n}(\vec{K},0)\sin\left[\frac{K^{2}L}{2k}\eta(1-\eta)\right]\sin\left[\frac{K^{2}L}{2k'}\eta(1-\eta)\right]. \tag{16}$$

As mentioned previously, the log-amplitude fluctuations are most sensitive to eddies the size of the Fresnel zone. Therefore, if the Fresnel zone is much smaller than the outer scale and much larger than the inner scale; i.e. $l_{0}\ll\mu\ll L_{0}$, then $\sqrt{K^{2}+K_{z}^{2}}\gg K_{0}$, $\Gamma\approx 1$, and the power spectrum in Eq. (14) can be approximated as the pure Kolmogorov spectrum:

$$\Phi_{n}(\vec{K},K_{z})\approx 0.033\,C_{n}^{2}\left(K^{2}+K_{z}^{2}\right)^{-11/6}. \tag{17}$$

In this case, Eq. (16) becomes:

$$C_{\chi}\left(\lambda,\lambda'\right)=0.033(2\pi)^{2}kk'LC_{n}^{2}\int_{0}^{1}\mathrm{d}\eta\int_{0}^{\infty}\mathrm{d}K \times K^{-8/3}\sin\left[\frac{K^{2}L}{2k}\eta(1-\eta)\right]\sin\left[\frac{K^{2}L}{2k'}\eta(1-\eta)\right]. \tag{18}$$

Following a bit of trigonometry, Eq. (18) becomes:

$$C_{\chi}\left(\lambda_{c},u\right)=0.033(2\pi)^{2}\frac{k_{c}^{2}LC_{n}^{2}}{1-u^{2}/4}\int_{0}^{1}\mathrm{d}\eta\int_{0}^{\infty}\mathrm{d}KK^{-8/3} \times\left\{\sin^{2}\left[\frac{K^{2}L}{2k_{c}}\eta(1-\eta)\right]+\frac{1}{2}\cos\left[\frac{K^{2}Lu}{2k_{c}}\eta(1-\eta)\right]-\frac{1}{2}\right\}, \tag{19}$$

where $\lambda_{c}=(\lambda+\lambda')/2$ is the central wavelength, $u=(\lambda-\lambda')/\lambda_{c}$ is the normalized wavelength difference, and $k_{c}=2\pi/\lambda_{c}$. Note that as the refractive index is a function of wavelength, C_{n}^{2} is also wavelength dependent [16]. However, assuming that the bandwidth is sufficiently narrow this dependence may be neglected.

Using the substitution $a=K\sqrt{L\eta(1-\eta)/(2k_{c})}$, Eq. (19) is simplified to:

$$C_{\chi}\left(\lambda_{c},u\right)=\frac{0.033(2\pi)^{2}}{2^{5/6}}\frac{k_{c}^{7/6}L^{11/6}C_{n}^{2}}{1-u^{2}/4}\int_{0}^{1}\mathrm{d}\eta\left[\eta(1-\eta)\right]^{5/6}\int_{0}^{\infty}\mathrm{d}a\,a^{-8/3} \times\left\{\sin^{2}\left[a^{2}\right]+\frac{1}{2}\cos\left[a^{2}u\right]-\frac{1}{2}\right\}, \tag{20}$$

while using the substitution $b = a\sqrt{|u|}$ gives:

$$C_\chi(\lambda_c, u) = \frac{0.033(2\pi)^2}{2^{5/6}} \frac{k_c^{7/6} L^{11/6} C_n^2}{1 - u^2/4} \int_0^1 \mathrm{d}\eta \left[\eta(1-\eta)\right]^{5/6} \times \left\{ \int_0^\infty \mathrm{d}a\, a^{-8/3} \sin^2\left[a^2\right] - \frac{|u|^{5/6}}{2} \int_0^\infty \mathrm{d}b\, b^{-8/3} \left(1 - \cos\left[b^2\right]\right) \right\} . \quad (21)$$

After evaluating the two integrals, Eq. (21) reduces to:

$$C_\chi(\lambda_c, u) = \sigma_\chi^2(\lambda_c) \frac{1 - 0.561\,|u|^{5/6}}{1 - u^2/4} ; \quad (22)$$

where:

$$\sigma_\chi^2(\lambda_c) = 0.124 k_c^{7/6} L^{11/6} C_n^2 , \quad (23)$$

is the log-amplitude variance for a spherical wave with wavelength λ_c propagating through Kolmogorov turbulence. Interestingly, this means that the log-amplitude correlation function, R_χ, depends only on the normalized wavelength difference:

$$R_\chi(u) = \frac{C_\chi(\lambda_c, u)}{\sqrt{\sigma_\chi^2(\lambda)\,\sigma_\chi^2(\lambda')}} = \frac{1 - 0.561\,|u|^{5/6}}{(1 - u^2/4)^{5/12}} . \quad (24)$$

Its plot in Fig. 2 shows that it can be substantially reduced (< 0.5) for a normalized wavelength difference greater than 1. Note that if the linear approximation $C_I \approx 4C_\chi$ holds, then the log-amplitude correlation function is identical to the irradiance correlation function, i.e. $R_I(u) = R_\chi(u)$.

2.3 Bandwidth variance

In order to properly analyze the measurement data, let's consider the variance of irradiance that is integrated about a central wavelength Λ with a bandwidth $\delta\lambda$. For the linear approximation, this is defined as:

$$V(\Lambda, \delta\lambda) = \int_a^b \mathrm{d}\lambda \int_a^b \mathrm{d}\lambda' C_I(\lambda, \lambda') \approx 4 \int_a^b \mathrm{d}\lambda \int_a^b \mathrm{d}\lambda' C_\chi(\lambda, \lambda') , \quad (25)$$

where $a = \Lambda - \delta\lambda/2$ and $b = \Lambda + \delta\lambda/2$. Now writing the variable u in Eq. (22) as $u = (\Lambda/\lambda_c)(\lambda - \lambda')/\Lambda$, gives:

$$C_\chi(\lambda, \lambda') = \sigma_\chi^2(\Lambda) \left(\frac{\Lambda}{\lambda_c}\right)^{\frac{7}{6}} \frac{1 - 0.561(\Lambda/\lambda_c)^{5/6}(|\lambda - \lambda'|/\Lambda)^{5/6}}{1 - (1/4)(\Lambda/\lambda_c)^2(|\lambda - \lambda'|/\Lambda)^2} ; \quad (26)$$

which simplifies to:

$$C_\chi(\lambda, \lambda') = \sigma_\chi^2(\Lambda) \frac{\left(\frac{\lambda_c}{\Lambda}\right)^{\frac{5}{6}} - 0.561 \left(\frac{|\lambda - \lambda'|}{\Lambda}\right)^{\frac{5}{6}}}{\left(\frac{\lambda_c}{\Lambda}\right)^2 - \frac{1}{4}\left(\frac{|\lambda - \lambda'|}{\Lambda}\right)^2} . \quad (27)$$

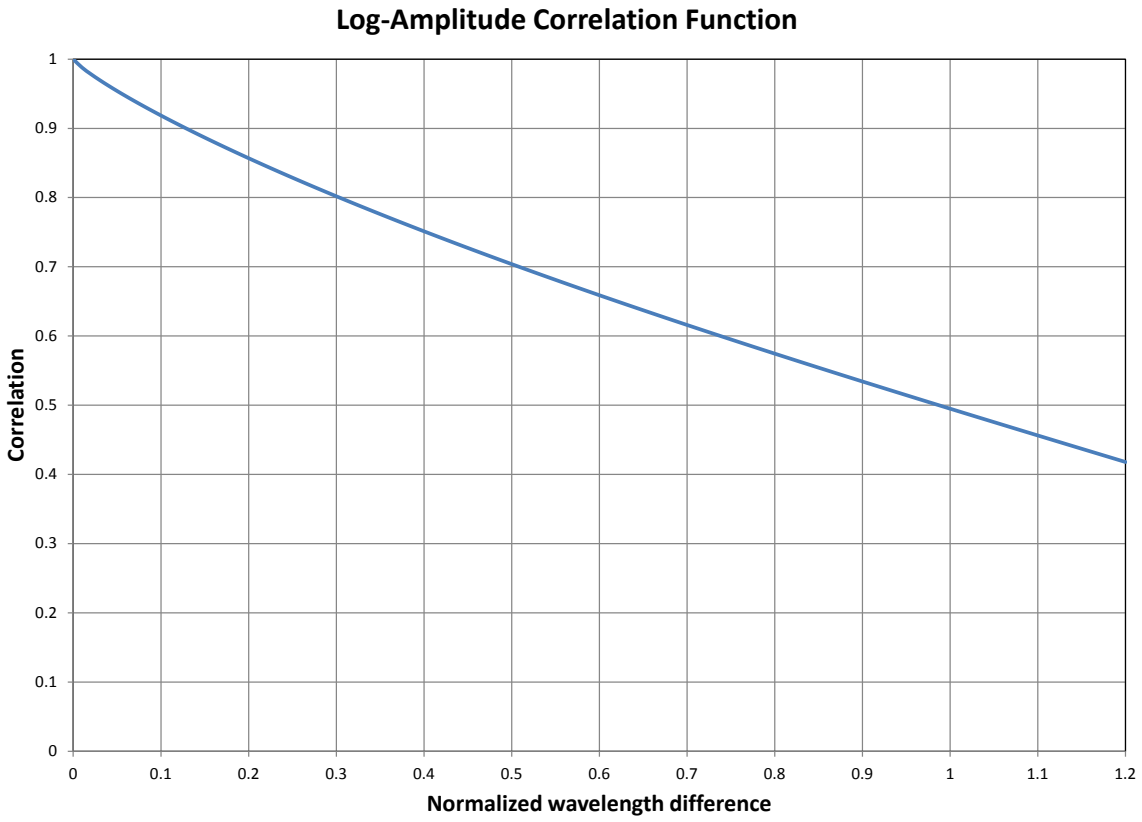

Figure 2: *Plot of the log-amplitude correlation function as a function of the normalized wavelength difference.*

Finally, as $\Lambda = (a+b)/2$, the following elegant expression is obtained:

$$C_\chi(\lambda, \lambda') = \sigma_\chi^2(\Lambda) \frac{\left(\frac{\lambda+\lambda'}{a+b}\right)^{\frac{5}{6}} - \left(\frac{|\lambda-\lambda'|}{a+b}\right)^{\frac{5}{6}}}{\left(\frac{\lambda+\lambda'}{a+b}\right)^{2} - \left(\frac{|\lambda-\lambda'|}{a+b}\right)^{2}}, \tag{28}$$

and the normalized irradiance variance is given by:

$$\widetilde{V}(\Lambda, \delta\lambda) = \frac{V(\Lambda, \delta\lambda)}{4\sigma_\chi^2(\Lambda)} = \int_a^b \mathrm{d}\lambda \int_a^b \mathrm{d}\lambda' \left\{ \frac{\left(\frac{\lambda+\lambda'}{a+b}\right)^{\frac{5}{6}} - \left(\frac{|\lambda-\lambda'|}{a+b}\right)^{\frac{5}{6}}}{\left(\frac{\lambda+\lambda'}{a+b}\right)^{2} - \left(\frac{|\lambda-\lambda'|}{a+b}\right)^{2}} \right\}. \tag{29}$$

An example of the normalized irradiance variance is plotted in Fig. 3, where it shows that for a central wavelength of 400 nm it can be approximated by the bandwidth squared; i.e. $(b-a)^2$. This means that the integrand in Eq. (29) is close to unity, at least for bandwidths of 50 nm or less, implying that the log-amplitude correlation function is also close to unity. This is seen in Fig. 2, where for a maximum normalized wavelength difference of

$u = 50/400 = 0.125$, the correlation is about 0.9.

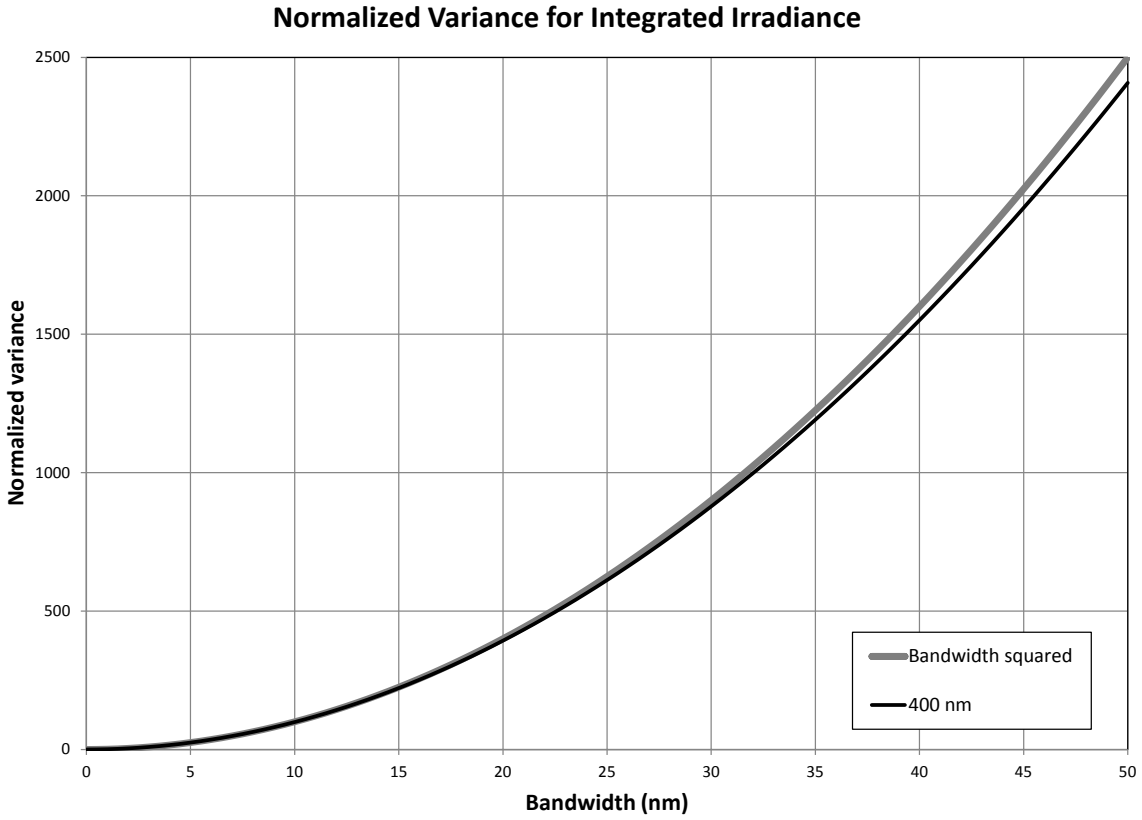

Figure 3: *Plot of the normalized variance of integrated irradiance for a central wavelength of 400 nm (black line) as a function of the bandwidth. The thick gray line is the bandwidth squared for comparison.*

3 The measurement trial

A measurement trial was held in DRDC – Valcartier Research Centre's AB-range from April 15 to May 5 2015. It was intended to test the hyper-spectral covariance caused by turbulence by propagating a coherent beam with a particular central wavelength and bandwidth through artificially generated turbulence. The AB-range is an indoor facility used for making ballistic tests on a variety of projectiles. It is a hallway about 250 m long, and was chosen because such a length is suitable for imaging tests. The fact that it is an indoor facility allows us to turn the artificial turbulence on or off as needed, which creates a turbulent and pristine version of the same scene. We begin by describing the apparatus used and its configuration for the trial in Section 3.1. We will then examine the actual data taken at the trial in Subsection 3.2 and compare it to the model developed in Section 2.3.

3.1 The measurement layout

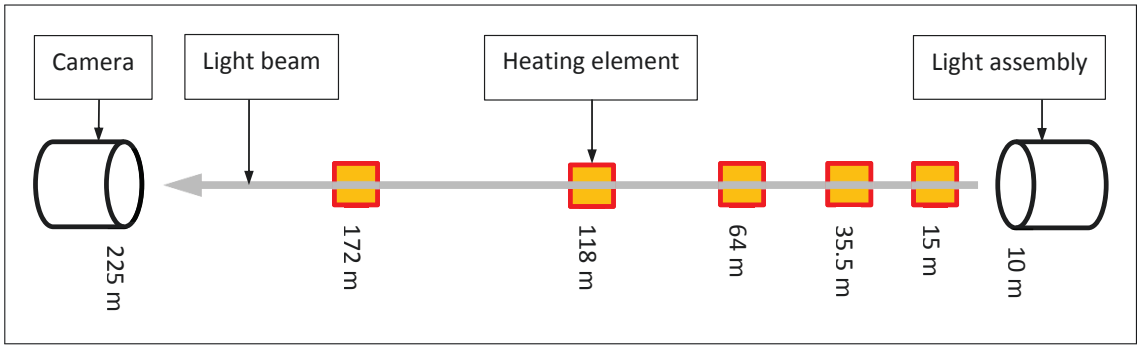

Figure 4: *An illustration of the layout of the equipment used along with their position along the AB-range. At the far right is the light assembly (integrating sphere + bandpass filter + Fresnel lens) located at about 10 m from the end of the range. The assembly creates a coherent beam which propagates to the camera at the far left. Along the way there are a series of heating element placed just under the beam.*

The basic layout of our experiment is illustrated in Fig. 4, where we see a light assembly at one end of the AB-range projecting a coherent beam through artificial optical turbulence to a high-speed panchromatic digital camera at the opposite end. The camera was a Mikrotron EoSens CL MC1632 and it was coupled to a Questar telescope having a 3.5" diameter aperture and a focal length of over 1 m. This is shown in Fig. 5. The light assembly is shown in Fig. 6, where we see a Labsphere 8" integrating sphere with spectralon interior and a blackbody lamp with an equivalent temperature of 3400 K. A bandpass optical filter is placed in front of the sphere's output, which is itself placed at the focal point of an 18" diameter Fresnel lens. This produces a coherent beam with a defined central wavelength and bandwidth.

Figure 5: *The Mikrotron digital camera mounted to a Questar telescope.*

Optical bandpass filters sets for central wavelengths of 450 nm, 500 nm, 550 nm, 600 nm, 650 nm and 700 nm were used. Each set consisted of three filters with bandwidths of 10 nm, 25 nm and 50 nm, for a total of 18 filters in all. For each filter, various image sequences were taken with all of the heating elements turned on, only one of the elements turned on at a time, or no element turned on (pristine image). All of the image sequences were acquired at a frame rate of 500 Hz over a period of 4 seconds.

3.2 Data analysis

For the purposes of this analysis, only the central wavelengths 550 nm, 600 nm, 650 nm and 700 nm were considered, as the beams at the other wavelengths were considered insufficiently bright to yield reliable data. Also, only cases with all of the heating elements turned on were analyzed, as this most closely corresponds to the model of Section 2.3. An example of this is displayed in Fig. 7, where a frame of a pristine sequence for a 600 nm central wavelength beam at a bandwidth of 25 nm is shown, along with a frame from the same beam for a sequence with all the heaters turned on.

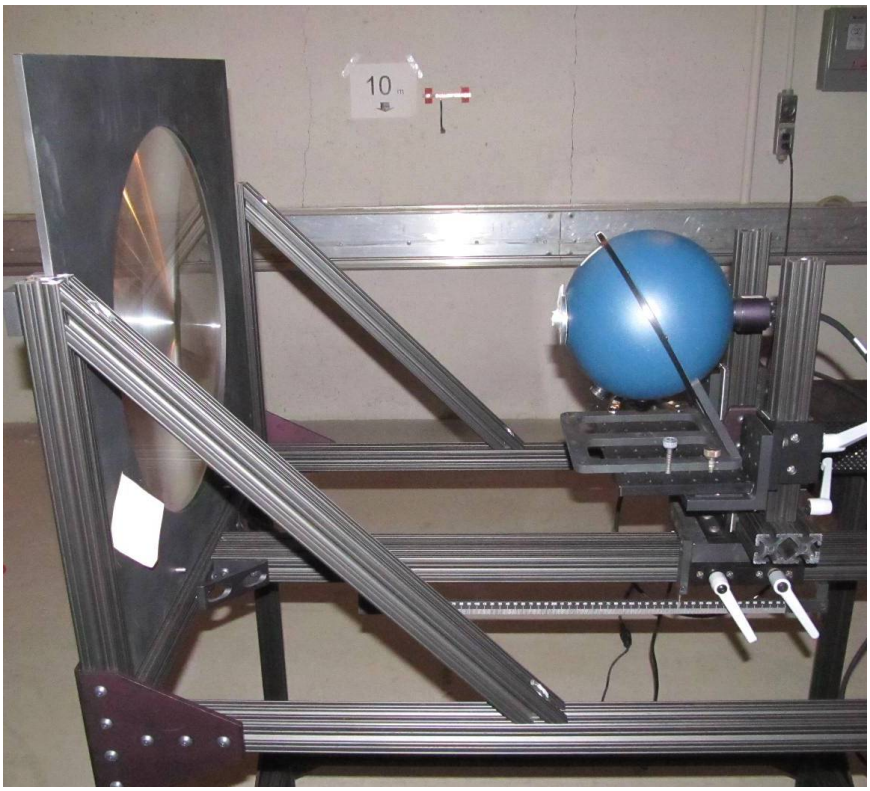

Figure 6: *The light assembly consisting of an integrating sphere with a bandpass optical filter at its output, which is placed at the focal point of a Fresnel lens.*

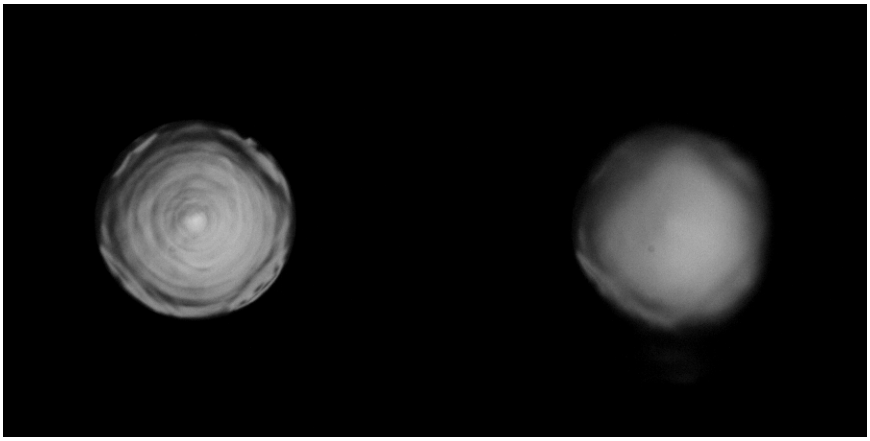

Figure 7: *A sample image from the non-turbulent sequence of the 600 nm central wavelength beam with a bandwidth of 25 nm (left) along with an image from the same beam from the turbulent sequence with all of the heaters turned on (right).*

The signal processing consisted of integrating the irradiance of the beam over the entire image, for each image in a sequence. This creates a time series of total irradiance for each sequence (an example of which is shown in Fig. 8). The covariance between the total irradiance values are then estimated for one time step difference, which is an interval of 2 msec. This estimate is used as the value of the total irradiance variance V_I without the noise from the camera. The Mikrotron MC1632 camera has three basics settings of image acquisition: black level, gain and shutter time. The shutter time, τ, is the exposure time for each image, the gain, G, simply multiplies the image intensity by a given factor, while the black level linearly increases or decreases the image intensity by a given amount.

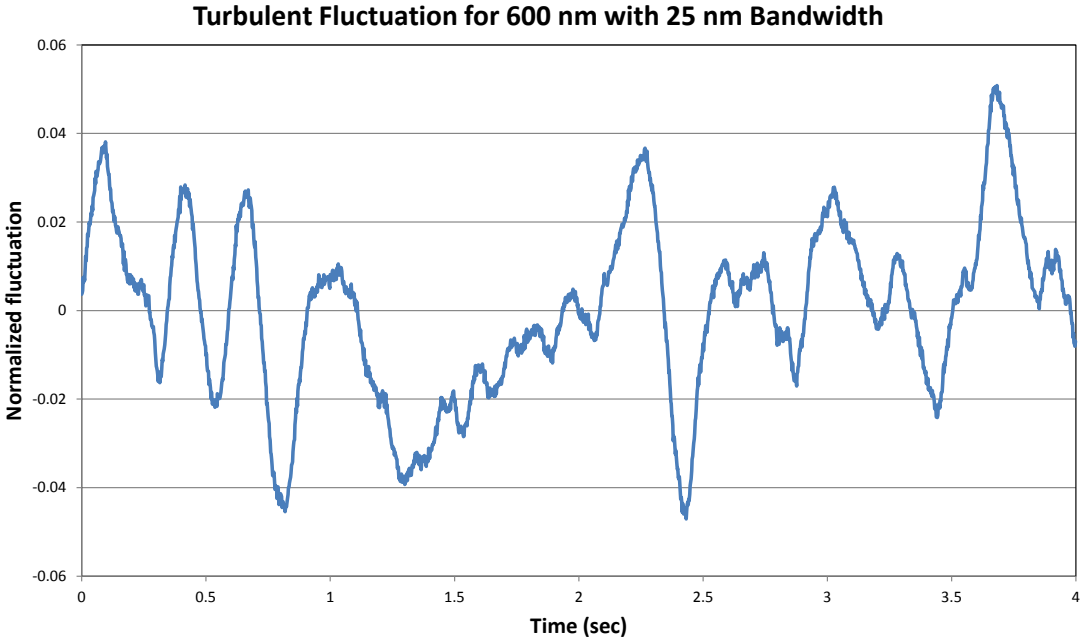

Figure 8: *The sequence of turbulent fluctuations with respect to the average for the 600 nm central wavelength beam with a bandwidth of 25 nm. The fluctuations are normalized as they are divided by the average.*

Since the average from the time series is removed to find the variance, the black level doesn't matter. Therefore, the bandwidth variance, V, from section 2.3 is proportional to the image variance as:

$$V(\Lambda, \delta\lambda) \propto \frac{V_I(\Lambda, \delta\lambda)}{G^2\tau^2}. \tag{30}$$

Note that the proportionality sign in Eq. (30) signifies that an exact equality depends on unknown factors depending on the camera and telescope assembly. Such concerns are eliminated by comparing the measured and modeled variance ratios for the same central wavelengths but for different bandwidths:

$$\frac{V(\Lambda, \delta\lambda')}{V(\Lambda, \delta\lambda)} = \left(\frac{G\tau}{G'\tau'}\right)^2 \frac{V_I(\Lambda, \delta\lambda')}{V_I(\Lambda, \delta\lambda)}. \tag{31}$$

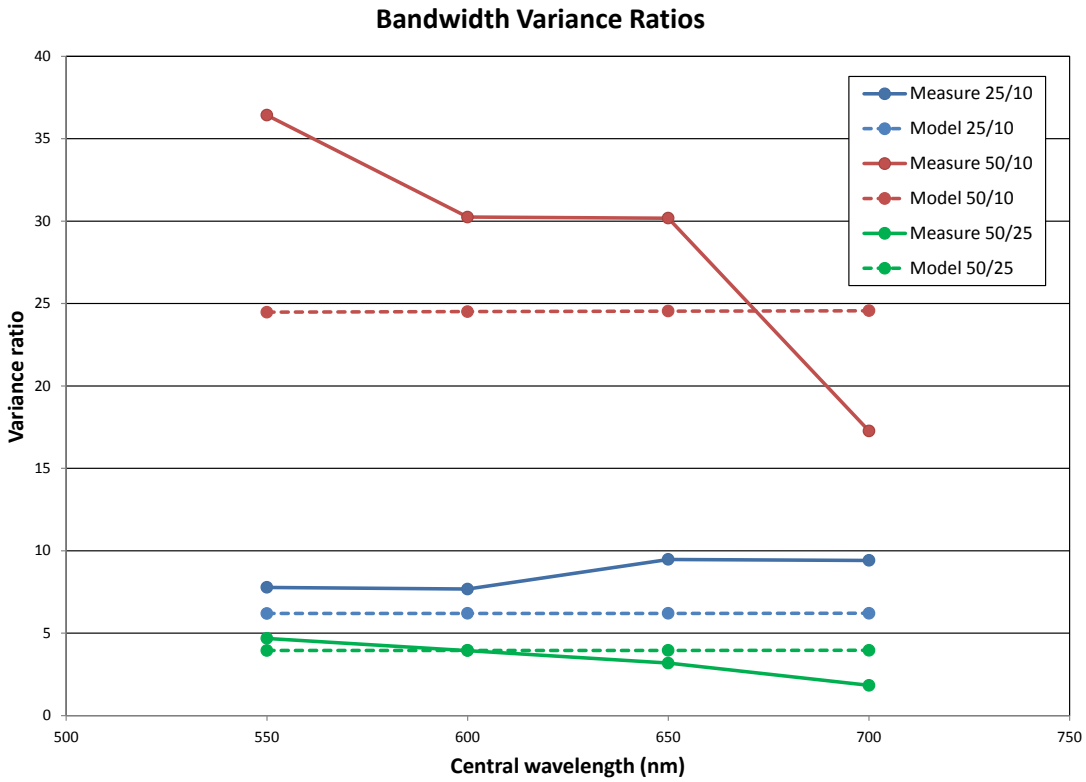

Figure 9: *The bandwidth variance ratios as a function of central wavelength. The solid lines represent the measurements and the dashed lines the model. The 25 nm to 10 nm ratios are represented in blue, the 50 nm to 10 nm ratios in red, and the 50 nm to 25 nm ratios are in green.*

Comparisons of measured and modeled bandwidth variance ratios are shown in Fig. 9. It shows that the measured values are roughly similar to the modeled values. Nevertheless, there are significant differences, particularly for the 550 nm and 700 nm central wavelengths.

These differences are hardly surprising given the discrepancies between the assumptions of the model and the measurement set-up. The beam is not a point source and is coherent, while the telescope is not a point receiver. Furthermore, while the heaters can produce strong optical turbulence, it is reasonable to assume that they cannot produce a Kolmogorov turbulent spectrum around the scale of the Fresnel zone (which is about from 1 to 1.2 cm for this set-up). Finally, the black level setting for the camera is not as simple as a linear shift in intensity. Tests have revealed that the camera performs some kind of non-linear operation for low-intensity values that is difficult to quantify and, therefore, to correct. This could have an effect on low-intensity images, such as those for 10 nm bandwidth beams that radiate less energy. Nonetheless, the results in Fig. 9 can be considered validate the model to some extent and to confirm its usefulness for describing turbulent variability in HSI.

4 Discussion and conclusions

In this work, the effects of optical turbulence on spectral variability for HSI have been investigated. This was done by creating coherent beams for various central wavelengths and spectral bandwidths, and propagating them through artificially generated optical turbulence. Image sequences of the beam were recorded with a panchromatic camera from which the turbulent variance of the total irradiance of the beams as a function of central wavelength and bandwidth were estimated.

A simple model for the spectral covariance induced by turbulence had been developed that allows a simple expression for the bandwidth variance to be obtained. Its results compare reasonably well with the measured variances; such that, in conclusion, the model can serve to describe turbulent variance for HSI under reasonably similar circumstances.

One scenario where the model may be of interest, would be that of an airborne platform looking down. Suppose that the platform is attempting to identify a target much smaller than the imager's pixel size, then such a target may be approximated as a point source. Furthermore, assuming that the target is set against a uniform Lambertian background (that is, uniform with respect to the size of a pixel), then the turbulence will only affect the spectrum of the target and not the background. This is because optical turbulence does not affect uniform Lambertian surfaces [17] on account of the energy conservation of the Green's function for electromagnetic propagation [18].

It therefore seems conceivable that turbulence may adversely affect target detection algorithms that use assumed values of spectral covariance. For instance, the Hyspex company makes Visible Near Infra-Red (VNIR) and Short Wave Infra-Red (SWIR) hyper-spectral cameras (see the web site in Ref. [19]); where the VNIR has a wavelength band from 400 nm to 1 μm, and the SWIR has a wavelength band from 1 μm to 2.5 μm. Both of these cameras have a maximum normalized wavelength difference of 0.86, which, according to Fig. 2, means that there is a correlation of about 0.55 between the minimum and maximum wavelengths.

This is a significant loss of correlation. However, in the airborne scenario almost all of the turbulence is concentrated near the ground, thereby making the effective C_n^2 very small and reducing the spectral covariance. Adding effects such as the integration time of the camera and the aperture averaging, may even further reduce the covariance. Therefore, the extent to which turbulence may impede target detection algorithms for HSI remains to be seen. This would be an interesting topic for future work.

References

[1] Potvin, G. (2015), Average Turbulence Effects on Hyperspectral Imaging, Defence Research and Development Canada, Scientific Report, (DRDC-RDDC-2015-R004).

[2] Manolakis, D. and Shaw, G. (2002), Detection algorithms for hyperspectral imaging applications, *IEEE Signal Processing Mag.*, 19(1), 29–43.

[3] Stein, D. W. J., Beaven, S. G., Hoff, L. E., Winter, E. M., Schaum, A. P., and Stocker, A. D. (2002), Anomaly detection from hyperspectral imagery, *IEEE Signal Processing Mag.*, 19(1), 58–69.

[4] Manolakis, D., Truslow, E., Pieper, M., Cooley, T., and Brueggeman, M. (2014), Detection algorithms in hyperspectral imaging systems: An overview of practical algorithms, *IEEE Signal Processing Mag.*, 31(1), 24–33.

[5] Strohbehn, J. W. (1978), Modern Theories in the Propagation of Optical Waves in a Turbulent Medium, In Strohbehn, J. W., (Ed.), *Laser Beam Propagation in the Atmosphere*, pp. 45–106, Berlin: Springer-Verlag.

[6] Strohbehn, J. W. (1968), Line-of-sight wave propagation through the turbulent atmosphere, *Proc. IEEE*, 56, 1301–1318.

[7] Sancer, M. I. and Varvatsis, A. D. (1970), A comparison of the Born and Rytov methods, *Proc. IEEE*, 58, 140–141.

[8] Mano, K. (1970), Interrelationship between terms of the Born and Rytov expansions, *Proc. IEEE*, 58, 1168–1169.

[9] Clifford, S. F. (1978), The Classical Theory of Wave Propagation in a Turbulent Medium, In Strohbehn, J. W., (Ed.), *Laser Beam Propagation in the Atmosphere*, pp. 9–43, Berlin: Springer-Verlag.

[10] Beland, R. R. (1993), Propagation through Atmospheric Optical Turbulence, In Smith, F. G., (Ed.), *Atmospheric Propagation of Radiation*, pp. 157–232, Bellingham, Washington USA: SPIE Press.

[11] Potvin, G. (2015), General Rytov Approximation, *J. Opt. Soc. Am. A*, 32(10), 1848–1856.

[12] Potvin, G., Forand, J. L., and Dion, D. (2007), A Parametric Model for Simulating Turbulence Effects on Imaging Systems, Defence R&D Canada – Valcartier, Technical Report, (TR 2006-787).

[13] Churnside, J. H. (1990), A Spectrum of Refractive Turbulence in the Turbulent Atmosphere, *J. Mod. Opt.*, 37(1), 13–16.

[14] Williams, R. M. and Paulson, C. A. (1977), Microscale Temperature and Velocity Spectra in the Atmospheric Boundary Layer, *J. Fluid Mech.*, 83(3), 547–567.

[15] Champagne, F. H., Friehe, C. A., LaRue, J. C., and Wyngaard, J. C. (1977), Flux Measurements, Flux Estimation Techniques, and Fine-Scale Turbulence Measurements in the Unstable Surface Layer Over Land, *J. Atmos. Sci.*, 34(3), 515–530.

[16] Andreas, E. L. (1988), Estimating C_n^2 over snow and sea ice from meteorological data, *J. Opt. Soc. Am. A*, 5(4), 481–495.

[17] Potvin, G., Forand, J. L., and Dion, D. (2011), A Simple Physical Model for Simulating Turbulent Imaging, In Holst, G. C. and Krapels, K. A., (Eds.), *Infrared Imaging Systems: Design, Analysis, Modeling and Testing XXII*, Vol. 8014 of *Proc. SPIE*, pp. 80140Y–13.

[18] Charnotskii, M. (2012), Common Omissions and Misconceptions of Wave Propagation in Turbulence: Discussion, *J. Opt. Soc. Am. A*, 29(5), 711–721.

[19] HySpex Web Site (online), Norsk Elektro Optikk, http://www.hyspex.no (Access Date: March 2018).

DOCUMENT CONTROL DATA

*Security markings for the title, authors, abstract and keywords must be entered when the document is sensitive

1. ORIGINATOR (Name and address of the organization preparing the document. A DRDC Centre sponsoring a contractor's report, or a tasking agency, is entered in Section 8.)

DRDC – Valcartier Research Centre
2459 de la Bravoure Road, Québec
QC G3J 1X5, Canada

2a. SECURITY MARKING (Overall security marking of the document, including supplemental markings if applicable.)

CAN UNCLASSIFIED

2b. CONTROLLED GOODS

NON-CONTROLLED GOODS
DMC A

3. TITLE (The document title and sub-title as indicated on the title page.)

Turbulence variability in hyper-spectral imagery

4. AUTHORS (Last name, followed by initials – ranks, titles, etc. not to be used. Use semi-colon as delimiter)

Potvin, G.

5. DATE OF PUBLICATION (Month and year of publication of document.)	6a. NO. OF PAGES (Total pages, including Annexes, excluding DCD, covering and verso pages.)	6b. NO. OF REFS (Total cited in document.)
November 2018	22	19

7. DOCUMENT CATEGORY (e.g., Scientific Report, Contract Report, Scientific Letter)

Scientific Report

8. SPONSORING CENTRE (The name and address of the department project or laboratory sponsoring the research and development.)

DRDC – Valcartier Research Centre
2459 de la Bravoure Road, Québec QC G3J 1X5, Canada

9a. PROJECT OR GRANT NO. (If appropriate, the applicable research and development project or grant number under which the document was written. Please specify whether project or grant.)	9b. CONTRACT NO. (If appropriate, the applicable contract number under which the document was written.)
Project F3EAD 06be	

10a. DRDC DOCUMENT NUMBER	10b. OTHER DOCUMENT NO(s). (Any other numbers which may be assigned this document either by the originator or by the sponsor.)
DRDC-RDDC-2018-R257	

11a. FUTURE DISTRIBUTION WITHIN CANADA (Approval for further dissemination of the document. Security classification must also be considered.)

Public Release

11b. FUTURE DISTRIBUTION OUTSIDE CANADA (Approval for further dissemination of the document. Security classification must also be considered.)

12. KEYWORDS, DESCRIPTORS or IDENTIFIERS (Use semi-colon as a delimiter.)

Hyper-Spectral Imaging; turbulence; spectral covariance

13. ABSTRACT/RÉSUMÉ (When available in the document, the French version of the abstract must be included here.)

Hyper-Spectral Imaging (HSI) is subject to adverse atmospheric effects such as aerosols, gas mixtures and turbulence. Although aerosol and gas mixture effects on HSI performance have been studied, little is known about optical turbulence effects on HSI spectral variability.

This has now been investigated by propagating coherent beams at various central wavelengths and spectral bandwidths in the aero-ballistic range at the DRDC – Valcartier Research Centre, and propagating them through artificially generated optical turbulence. Image sequences of the beam were recorded with a panchromatic camera, and the turbulent variance of the total irradiance of the beams as a function of central wavelength and bandwidth were estimated.

A simple model for the spectral covariance induced by turbulence was developed that compares reasonably well with the measured variances at various central wavelengths and bandwidths. This result gives some confidence in our model, which predicts potentially significant loss of correlation for Visible and Near Infra-Red (VNIR) and Short Wave Infra-Red (SWIR) spectra. It is concluded that turbulence effects could have a significant impact on HSI target identification and that further study is required.

L'imagerie hyper-spectrale (HSI : Hyper-Spectral Imaging) est sujette à des effets atmosphériques défavorables tels que les aérosols, les mélanges de gaz et les turbulences. Bien que les effets des mélanges d'aérosols et de gaz sur les performances de systèmes HSI aient été étudiés, les effets de la turbulence optique sur la variabilité spectrale pour le HSI sont peu connus.

Ces effets ont été étudié en propageant des faisceaux cohérents à diverses longueurs d'onde centrales et bandes passantes spectrales dans le couloir aéro-balistique du RDDC - Centre de recherches de Valcartier, et en les propageant à travers la turbulence optique générée artificiellement. Les séquences d'images du faisceau ont été enregistrées avec une caméra panchromatique, et la variance turbulente de l'irradiance totale des faisceaux en fonction de la longueur d'onde centrale et de la bande passante a été estimée.

Un modèle simple pour la covariance spectrale induite par la turbulence fut développé qui se compare raisonnablement bien avec les variances mesurées à diverses longueurs d'onde centrales et largeurs de bande. Ce résultat donne une certaine confiance dans notre modèle, qui prédit une perte potentiellement importante de corrélation pour les spectres VNIR (Visible and Near Infra-Red) et SWIR (Short Wave Infra-Red). Nous concluons que les effets de la turbulence pourraient avoir un impact significatif sur l'identification des cibles pour le HSI et qu'une étude plus approfondie est nécessaire.